Resonant waveguide sensing made robust by on-chip peak tracking through image correlation

Kristelle Bougot-Robin, Wen Weija, Henri Benisty

Resonant waveguide sensing made robust by on-chip peak tracking through image correlation

K. Bougot-Robin,[1,4] W. Wen,[2,*] and H. Benisty[3,5]

[1]*Institute for Advanced Study, Hong Kong University of Science and Technology, Clear Water Bay, Kowloon, Hong Kong, China*

[2]*Department of Physics, Hong-Kong University of Science and Technology, Clear Water Bay, Kowloon, Hong Kong, China*

[3]*Laboratoire Charles Fabry, Institut Optique Graduate School, CNRS, Université Paris Sud, 2 avenue Fresnel, Campus Polytechnique, 91127 Palaiseau, France*

[4]*kristelle_robin@yahoo.fr*

[5]*henri.benisty@institutoptique.fr*

**phwen@ust.hk*

Abstract: We demonstrate a solution to make resonant-waveguide-grating sensing both robust and simpler to optically assess, in the spirit of biochips. Instead of varying wavelength or angle to track the resonant condition, the grating itself has a step-wise variation with typically few tens of neighboring "micropads." An image capture with incoherent monochromatic light delivers spatial intensity sequences from these micropads. Sensitivity and robustness are discussed using correlation techniques on a realistic model (Fano shapes with noise and local distortion contributions). We confirm through fluid refractive index sensing experiments an improvement over the step-wise maximum position tracking by more than 2 orders of magnitude, demonstrating sensitivity down to 2×10^{-5} RIU, giving high potential development for bioarray imaging.

OCIS codes: (280.1415) Biological sensing and sensors; (310.2785) Guided wave applications; (050.5745) Resonance domain; (110.2960) Image analysis; (070.6110) Spatial filtering.

References

1. K. Bougot-Robin, J.-L. Reverchon, M. Fromant, L. Mugherli, P. Plateau, and H. Benisty, "2D label-free imaging of resonant grating biochips in ultraviolet," Opt. Express **18**(11), 11472–11482 (2010).
2. A. M. Ferrie, Q. Wu, and Y. Fang, "Resonant waveguide grating imager for live cell sensing," Appl. Phys. Lett. **97**(22), 223704 (2010).
3. P. Y. Li, B. Lin, J. Gerstenmaier, and B. T. Cunningham, "A new method for label-free imaging of biomolecular interactions," Sens. Actuators B Chem. **99**(1), 6–13 (2004).
4. R. Magnusson, D. Wawro, S. Zimmerman, and Y. Ding, S. Zimmerman, and Y. Ding "Resonant photonic biosensors with polarization-based multiparametric discrimination in each channel,"," Sensors (Basel Switzerland) **11**(2), 1476–1488 (2011).
5. E. M. Yeatman, "Resolution and sensitivity in surface plasmon microscopy and sensing," Biosens. Bioelectron. **11**(6-7), 635–649 (1996).
6. A. Shalabney and I. Abdulhalim, "Sensitivity enhancement methods for surface plasmon sensors," Laser Photonics Rev. **5**(4), 571–606 (2011).
7. S. George, I. D. Block, S. I. Jones, P. C. Mathias, V. Chaudhery, P. Vuttipittayamongkol, H. Y. Wu, L. O. Vodkin, and B. T. Cunningham, "Label-free prehybridization DNA microarray imaging using photonic crystals for quantitative spot quality analysis," Anal. Chem. **82**(20), 8551–8557 (2010).
8. S. S. Wang, R. Magnusson, J. S. Bagby, and M. G. Moharam, "Guided-mode resonances in planar dielectric-layer diffraction gratings," J. Opt. Soc. Am. A **7**(8), 1470–1474 (1990).
9. U. Fano, "Effects of configuration interaction on intensities and phase shifts," Phys. Rev. **124**(6), 1866–1878 (1961).
10. D. Pietroy, A. V. Tishchenko, M. Flury, and O. Parriaux, "Bridging pole and coupled wave formalisms for grating waveguide resonance analysis and design synthesis," Opt. Express **15**(15), 9831–9842 (2007).
11. B. Gallinet and O. J. F. Martin, "Influence of electromagnetic interactions on the line shape of plasmonic Fano resonances," ACS Nano **5**(11), 8999–9008 (2011).

12. B. Gallinet and O. J. F. Martin, "Ab initio theory of Fano resonances in plasmonic nanostructures and metamaterials," Phys. Rev. B **83**(23), 235427 (2011).
13. N. Destouches, B. Sider, A. V. Tishchenko, and O. Parriaux, "Optimization of a waveguide grating for normal TM mode coupling," Opt. Quantum Electron. **38**(1-3), 123–131 (2006).
14. L. Li, "Formulation and comparison of two recursive matrix algorithms for modeling layered diffraction gratings," J. Opt. Soc. Am. A **13**(5), 1024–1035 (1996).
15. A. David, H. Benisty, and C. Weisbuch, "Fast factorization rule and plane-wave expansion method for two-dimensional photonic crystals with arbitrary hole-shape," Phys. Rev. B **73**(7), 075107 (2006).
16. M. C. Estevez, M. Alvarez, and L. M. Lechuga, "Integrated optical devices for lab-on-a-chip biosensing applications," Laser Photonics Rev. **6**(4), 463–487 (2012).
17. T. K. Fang and T. N. Chang, "Determination of profile parameters of a Fano resonance without an ultrahigh-energy resolution," Phys. Rev. A **57**(6), 4407–4412 (1998).
18. X. Liu, Y. Huang, L. Zhu, Z. Yuan, W. Li, and K.-Z. Xu, "Numerical determination of profile parameters for Fano resonance with definite energy resolution," Nucl. Instrum. Methods Phys. Res. **508**(3), 448–453 (2003).
19. K. A. Tetz, L. Pang, and Y. Fainman, "High-resolution surface plasmon resonance sensor based on linewidth-optimized nanohole array transmittance," Opt. Lett. **31**(10), 1528–1530 (2006).
20. I. Abdulhalim, M. Auslender, and S. Hava, "Resonant and scatterometric gratings based nano-photonic structures for biosensing," J. Nanophotonics **1**(1), 011680 (2007).
21. O. Krasnykov, M. Auslander, and I. Abdulhalim, "Optimizing the guided mode resonance structure for optical sensing in water," Phys. Express **1**(0), 183–190 (2011).
22. X. Gan, N. Pervez, I. Kymissis, F. Hatami, and D. Englund, "A high-resolution spectrometer based on a compact planar two dimensional photonic crystal cavity array," Appl. Phys. Lett. **100**(23), 231104 (2012).

1. Introduction

Resonant waveguide grating (RWG) techniques offer a versatile capability for sensing at surfaces, for instance for label-free detection of the immobilization of biomolecules in the context of biochips or for sensing a minute amount of analyte. They make use of the "reservoir" nature of a guided wave and of its specific dispersion $\omega(k)$ to get an enhanced sensitivity to the grating surface condition, e.g., its local index of refraction. These techniques now have a broad range of proposed application. Even though very few have gone commercial, their capability to address any wavelength range including relatively deep-UV [1] and to comply with many variants such as chromatic or angular detection, is promising [2–4]. These techniques compete in several cases with the mature surface plasmon resonance technique (SPR) [5]. However, this latter requires a large apparatus with an equivalent angle scan, and is not implemented in "small" biochips, rather the fluidics is built around the typical prism basis used in SPR. Grating coupled SPR configuration is also possible. However, the sensitivity is 4 times lower than with prism coupling, allowing a 1×10^{-4} RIU (Refractive Index Unit) sensitivity for 0.2% noise vs. optical power, for the usual gold layer structure [6]. Multiplex SPR exists but is not easier to fully marry with the biochip paradigm.

In this work, we demonstrate a scheme featuring a number of the advantages in RWG sensing together with simple imaging setup. RWGs sensing is based on the change of resonance condition induced by a change of refractive index occurring at the chip surface (induced by bulk medium or biological layer recognition). This change is commonly measured through the shift of resonance wavelength or resonant angle [2–4,7]. An alternative is to measure the change in intensity for a fixed (λ_0, θ_0) configuration through imaging [1], but it is less robust than profile measurement. Figure 1(a) illustrates resonant profiles as a function of a general parameter u in both continuous and discrete forms. In Fig. 1(b), we report these same profiles in gray intensity level for more intuitive representation of what will be further described. The refractive index variation may be retrieved from the profile's shift measurement Δu_{res}, involving some adequate analysis to allow a precise measurement that encompasses the discreteness of the measured curve.

Our alternative option to the common angular or spectral versions is to scan a parameter of the grating itself, so that the resonant profile is straightforwardly captured with a camera and a monochromatic collimated source. In the discrete case more studied here, the units with neighboring resonant conditions are called "micropads" and each of their ensembles "a track" (see Fig. 1(b)). A track image, discrete or continuous, allows sensing much as a spectral or

angular scan would. Thus the sensing curves of Figs. 1(c) and 1(d) still give a proper basis for tracks' spatal profiles. The refractive index is determined from spatial position of the resonance peak on the chip or track instead of external instrumentation. The most profound advantages of this "peak tracking chip" technique, to our eyes, rest with the self-calibrated aspect of our sensor, i.e., the fact that a whole scan through resonance implies a signal shape analysis rather than a far less robust signal value easily plagued by drifts. The amount of data needed per sensing point (one track) does not sacrifice the capability to perform widely multiplex assays: in nowadays imaging, whereby pictures of 10 Mpixels are commonplace, allocating typically 20-50 Kpixels for one sensor still leaves room for over a hundred distinct (multiplex) track units.

We will show experimental realization of this peak-tracking chip technique: operating at λ~550 nm, with our chosen step-wise variation of the RWG duty-cycle (ratio of feature dimension to grating period Λ, also called filling factor *f*), we will perform index sensing down to ~2×10^{-5} RIU (refractive index unit) sensitivity. We shall also develop a model to justify that, as observed in practice, the sensing resolution shrinks, by more than two orders of magnitudes below the step $\Delta m = 1$ between two micropads. This point is important not only because accuracy is generally welcome, but also because it positively ensures that current lithography techniques can be used in spite of their inability to define subnanometer steps in gratings ridge/groove dimensions. We will further demonstrate the superiority of a correlation treatment over more conventional ones, using a control template (reference image) and the signal image to determine resonance shifts down to Δm~0.005, thus equivalent to such a subnanometer RWG pattern variation. Robustness of this correlation scheme to variations such as the change of waveguide thickness or grating depth modifying the Fano resonance shape, is another asset. Eventually, robustness to distortions and aberrations that we also observe in some real RWG assays shall also be evidenced.

The outline of the paper is as follows: in Section 2, we present a model of the system, including a discussion of a realistic implementation with duty-cycle variation. In Section 3, we present the correlation analysis and use it to assess the large degree of robustness. In Section 4, we apply our analysis approach to our fabricated structure and discuss it based on experimental results.

2. Model of stepped duty-cycle peak tracking resonance detection

2.1. Resonant waveguide and discretization

The principles of RWG resonances are well-known [8]. The exact RWG resonance for a plane wave impinging and an order p (often p = ±1) is given by Eq. (1):

$$k_0 \sin\theta_{\text{inc}} + pG_0 = k_0 N_{\text{eff}}(\lambda) = k_{\text{guid}}(\lambda), \tag{1}$$

where θ_{inc} is the angle of incidence, $k_0 = 2\pi/\lambda$ is the vacuum wavevector of incident light at vacuum wavelength λ, $G_0 = 2\pi/\Lambda$ is the grating wavevector, and $n_{\text{eff}}(\lambda)$ is the guided mode effective index in the adequate polarization of wavevector $k_{\text{guid}}(\lambda)$. The reflected intensity I has a singular behavior, often akin to a Fano resonance (Fig. 1(a)) around this exact resonance condition [9–12]. It is usually scanned through wavelength or angle. When sensing large index variations, for instance, it is enough to track the shift of peak position by Δu_{res}, as shown on Fig. 1(c), and signal-to-noise considerations may be superfluous. Conversely, when a small shift has to be detected, Fig. 1(d), e.g., to get the ultimate sensing sensitivity, refined analysis is needed.

The idea exploited in this paper is to measure as an approximation the resonance intensity profile $I(u-u_{\text{res}})$, not by scanning $u \equiv \theta$ or $u \equiv \lambda$, but by scanning by steps a grating parameter among $\{\Lambda, n_{\text{eff}}\}$, the effective index being itself sensitive to all the optogeometric grating parameters. For a rectangular-profile (lamellar) grating of period Λ, these parameters are waveguide layer thickness t, etch depth h, filling factor f, refractive index n_{ridge} of the ridges

(or of the grooves if they are not void). Curves given in Fig. 1 (a-d) correspond to our structure and fabrication-limited discretization, limited on a technology basis to be step-wise. However, let us remind here that our theory is general and that this present choice is only for presentation purpose. The continuous and discrete intensities correspond to profiles given in Fig. 1(a) but the gray scale image as in Fig. 1(b) is preferred throughout our work to represent the spatial dimension of our chip imaging technique. More details on our structure will be given later. We shall adopt in this paper the choice of a duty-cycle variation along the tracks using a row of M homogeneous micropads to obtain discrete profiles around the resonance, but it is not needed before Section 2. We will simply assume here that the intensity reflected in a relevant order (say, 0 or ±1) is a Fano-shaped resonance parameterized by a full width Γ_{res} and a Fano parameter q as given in Eq. (2).

$$\frac{I_{refl}}{I_{inc}} \propto \frac{(q\Gamma_{res}/2 + u - u_{res})^2}{(\Gamma_{res}/2)^2 + (u - u_{res})^2}. \qquad (2)$$

Depending on the scanning parameter u, the sign of q might be positive or negative. Typical Fano curves are given in Fig. 1(e) for $q = 1$, $q = 1.5$, $q = 2.5$, $q = 3.5$ and $q = 6$, q~3.5 profile resembling the one of our fabricated structure. As q increases, the curve symmetry increases.

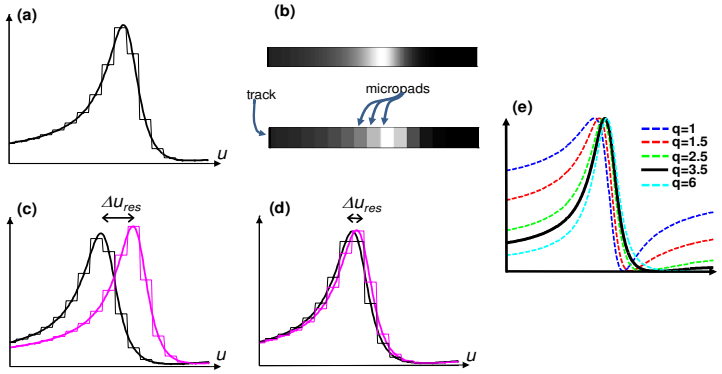

Fig. 1. (a) Generic resonance response in continuous and discretised form (b) Same as in (a) but in image intensity level (c, d) Shift of the resonance response resulting from a change of refractive index at the chip surface respectively for large Δn and small Δn (e) Fano shape for q parameters $q = 1$, $q = 1.5$, $q = 2.5$, $q = 3.5$ and $q = 6$, tending to a more symmetrical shape as q increases. Data from our structure resemble q~3.5.

Focusing now solely on sensing a refractive index change Δn, and assuming that the micropads behave like infinite gratings, we get the signals of Fig. 1(c,d) that we can denote $S(m) = I_{refl}(m)/I_{inc}$. $S(m)$ is a series of M normalized intensities associated to a series of M varying resonance conditions $u_{res}(m)$ obtained for a given analyte and for a fixed (λ_0,θ_0) illumination condition, practically a constant incidence collimated beam (nearly normal) and a nearly monochromatic incoherent source.

The simplest case is a constant shift of the resonance condition, such that the whole set $u_{res}(m)$ becomes a shifted set $u'_{res} = u_{res}(m-\Delta m)$ and $I(u-u_{res})$ becomes $I(u-u'_{res})$ with a linear relation $\Delta m = \Delta m_{res} = A\ S_{RIU}\ \Delta n$, where A is a constant, S_{RIU} a sensitivity to a given (sensed) index and Δn is the fluid index variation, or its equivalent for surface binding of monolayers of biomolecules. If the Δm versus Δn relation is not linear, a simple calibration shall work.

In this still realistic context, sensing consists of determining Δm as accurately as possible, by comparing the signal from the same track without $[u_{res}(m)]$ and with $[u_{res}(m-\Delta m)]$ the fluid index. Alternatively, adjacent tracks with reference and sensed fluids can be used so that pictures are taken simultaneously, cancelling thermal or mechanical drifts such as pressure stress in biochips. This parallel rather than sequential measurement will be our choice in the

following. Typical numbers as in Fig. 1(a-d) are a shift by Δm~30 to 40 micropads of our track profile from the lower fluid index (generally water n_{min} = 1.333) to the highest index fluids, say glycerol solutions with n_{max} = 1.474. In this way, as argued from Fig. 1(b) above, a coarse estimate is given by the discretized shift of the locus of maximum signal, amounting to bracket a fractional shift between two consecutive integers $[\Delta m] < AS_{RIU}\Delta n_{fluid} < [\Delta m] + 1$. Clearly, that would limit the accuracy to about $(n_{max}- n_{min})/\Delta m$, hence $\Delta n \approx 0.004$, in our case with Δm ~37, an insufficient sensitivity.

2.2. Duty-cycle variation for linear shift in track

We now detail in Fig. 2 a particular implementation of this general principle. Figure 2(a) gives a scheme of a track composed of M = 43 micropads. Micropad typical dimensions are 200µm × 90µm, with 10 µm distance between two successive micropads. These dimensions may however be decreased for higher bioarray density. Their RWG are designed for imaging close from sample normal at a green wavelength λ. Their structure is shown in Fig. 2(b). It consists of a borosilicate glass substrate (n = 1.4713, provider data) covered by a PECVD silicon nitride layer of index n = 2.10 + 0.0026i (determined by ellipsometry), structured by gratings of period Λ = 450 nm. The silicon nitride layer of deposited thickness t = 0.27Λ, is etched on a depth h = 0.15Λ. These parameters may be further optimized but are already suitable for good sensitivity [13]. To span around the resonance, we vary the filling factor of micropads $f_m = d_m/\Lambda$, with d_m the groove width ($1 \le m \le M$) while other parameters (period Λ, waveguide layer thickness t, etching depth h) are kept constant. The groove width is varied between 140 nm to 308 nm by step Δd_m = 4 nm, corresponding to filling factor varying from 0.3 to 0.7 by step Δf_m = 0.0089. Such a variation is at technological limits of our e-beam lithography system. Grooves are along the track direction so that the guided mode of one micropad does not travel to its neighbor.

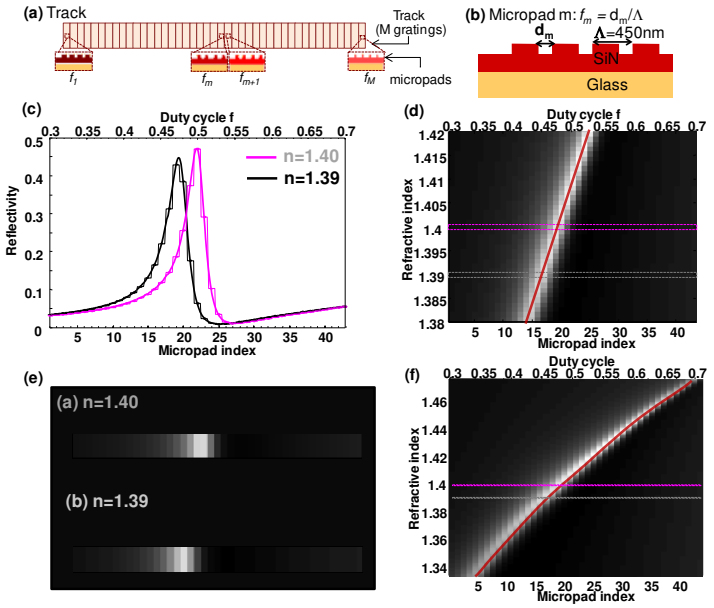

Fig. 2. (a) Scheme of a track composed of M gratings micropads of varying filling factor f_m from f_1 = 0.3 to f_M = 0.7; (b) Side-view of micropad RWG structure; (c) Simulated reflectivity spectrum with sensed media of index n = 1.39 and n = 1.40 respectively; (d) Simulated reflectivity map through the range n = 1.38-1.42 on a [0-0.5] gray level scale; (e) Ideal images (noise free, distortion free) of tracks sensing n = 1.39 and n = 1.40 medium on a [0-0.5] scale. Images shown actually correspond to the 2 slices reported on reflectivity maps; (f) Simulated reflectivity map on the range n = 1.333-1.474 on a [0-0.5] scale, showing modest resonance position curvature that may be corrected by prior calibration.

The RWG reflectivities for the illumination condition (λ = 558 nm, θ = 18°) are calculated using a scattering matrix method formalism [14,15], for different cover (analyte) refractive indices. Figure 2(c) gives the responses (specular reflected intensities) as a function of a continuous or a discrete version of the duty-cycle variation, for n = 1.39 or n = 1.40. The full map of profiles on the range [1.38-1.42] is given in Fig. 2(d) and shows additionally the linearity of micropad resonance position vs. analyte index, a favorable property of the duty-cycle variation. To give a more precise idea of images, we illustrate two "tracks" in Fig. 2(e) that are the two ideal (noise-free, distortion-free) images according to the profiles on Fig. 2(c): one may serve as a control/reference and the other as sensing area, and the shift has to be quantified as suggested in Fig. 1. Figure 2(f) shows the reflectivity map on a larger range [1.333–1.474]. We see that a modest curvature of the response exists for a larger index span, easy to calibrate. Note that on Fig. 2(f) as well as on Fig. 2(c) due to the different electromagnetic conditions, the intensity of reflectivity at resonance peak differ, typically spanning a factor of two between the extremes n ~ 1.333 and n ~ 1.474, hence still leaving absolute signals and, e.g., photon noise contribution, in the same range.

The self-referenced aspect of the technique is of foremost importance to ensure precise measurement, notably with our choice mentioned above of using two adjacent tracks rather than a sequential measurement. For biological detection, in the framework of bioarray, a control track may also be used for unspecific binding correction. In general, with a large image sensor, the possibility of having an N × P tracks array for multiplexing opens a large range of bio-sensing applications. Although current track dimensions are of ~200µm × 4.3mm, smaller dimensions may suffice, particularly if the index span Δn is small: for instance in many cases a thin biological layer induces a less than 10^{-2}–10^{-3} equivalent RIU change, so on the order of $\Delta m \sim 1$ micropad shift. The row alignment of micropads may also be replaced by different spatial arrangement.

2.3. Fitting issues with Fano line shapes

We now want to show that the accuracy is a small fraction of a micropad, say down to $\Delta m \sim 0.005$, which shall allow our chip-oriented method to serve at $\Delta n \approx 2 \times 10^{-5}$, nearly the same degree of accuracy as bulky Abbe's refractometers, but with a lot of versatility, and without any of the ambiguities of the Mach-Zehnder methods [16].

It is well-known that, generically, the accuracy in peak position can be much less than peak width if signal-to-noise ratio is large enough to ensure that the centroid of the peak can be pointed precisely. However, Fano peaks are not so obvious to analyze [11,12,17–19].

Increase in sensitivity may be obtained by fitting data to known models or using a correlation approach, by correlating the signal image (whose shift we want to determine) with the reference image. We will give further justification of choosing the correlation approach later. First, using simulated data with our structure parameters, we will demonstrate the superiority of a correlation approach against Gaussian and Lorentzian shape fitting. Later, we will see that this approach also achieves a high immunity to parasitic contributions (noise, distortion from various origins).

In Fig. 3, we give a justification of a correlation approach that we have found to be superior to other methods. Figure 3(a) gives reflectivity map on the range [1.38–1.42], with here dashed lines showing a selection of three data set associated to a compounded $\Delta n = 10^{-3}$ index step. The corresponding data are the gray dots in Fig. 3(b,c). On these data, a naïve Gaussian fit gives very poor results: the fits themselves on Fig. 3(b) make it clear that a Gaussian fit is fooled by the different behavior of the peak and of the tails. Consequently, as seen by the wavy line in Fig. 3(a), such a fit is heavily affected by the discretization. A home-made Lorentzian fit based on fitting the inverse of the signal as a parabola, and restricting the fit to the set of points underlined by the thick dashed line in Fig. 3(c), has a less wavy overall behavior, as is seen on Fig. 3(a), although shifted systematically to lower index as a

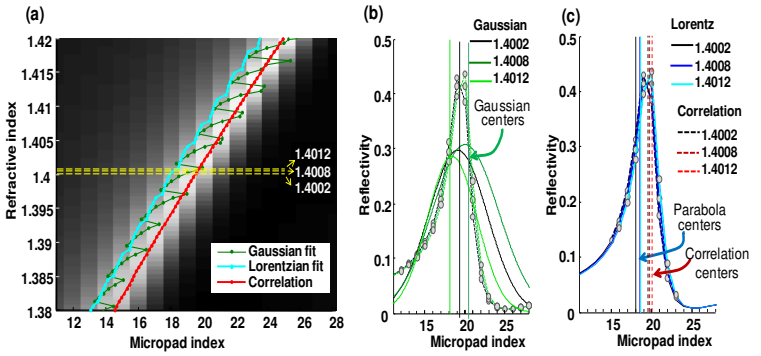

Fig. 3. (a) Gray level map of resonances as a function of micropad index and refractive index. Resonance position determined by fitting together with the correlation-based determination are reported on the map, with poorer accuracy for the two fit options. The three values indicated near n = 1.400 by yellow dashed lines indicate the reflectivities plotted in (b) for Gaussian fit and (c) for Lorentzian fit. They give poor tracking of the Fano resonance resulting in low accuracy in resonance position determination (see non-linearity of the peak position bars).

consequence of the asymmetry of Fano profile being improperly dealt with and with inconstant step between successive points.

We do not claim here that these fits are optimized. But we see that fitting a Fano resonance from standard engineering approaches shall certainly require many refinements before it gives a good result. And furthermore, this result shall depend on the asymmetry (factor q) of Fano shape in play, which may vary on a chip between, for instance, extreme refractive indices. Therefore, a more suited approach is welcome. The red line, on Fig. 3(a), is the resonant peak position retrieved by correlation approach that we have devised, and that we believe to overcome most of the cited limitations of fitting. Peak position is also reported with bars in Fig. 3(c) for the selected profiles.

Before applying this correlation method to our experimental results, we give in Section 3 a theoretical outline of its robust behavior.

3. The correlation approach and its performance estimation

3.1. Resonance shift analysis with correlation approach

Determination of Fano parameters requires some modeling and numerical analysis. Instrumental function (especially in resolution limited cases…) as well as discretization and truncation effects must be considered [17–19]. Recent efforts have been made to characterize and determine Fano parameters from optical responses; and more particularly in plasmonic nanostructures [11,12]. Sufficient instrumental resolution is however necessary for accurate fitting. In view of refractive index determination, we will mainly be interested in the determination of resonance position. Our main issue is discretization, which can be viewed as a particular flavor of limited resolution, but not in the usual sense of a convolution by an instrument function. The following addresses this issue by a correlation approach well suited to such discretized Fano line shapes and discusses its robustness to parasitic contributions such as noise or other optical effects (from chip or instrumentation setup). Although various tests were performed with different Fano parameters q from 1 to 6 and confirmed the wide validity of correlation analysis, we only present Fano parameter $q = 2.5$ results to illustrate a signal with no particular odd or even symmetry.

To analyze large amount of data in our noise assessments, we worked at a slightly lower number of pixels per micropads than in experimental data presented in Section 4, but the results are pretty independent of these exact numbers. One can imagine some kind of 2×2 binning with no conceptual consequence. We therefore deal with the model data similar to those in Fig. 2(e) with now $D_x \times D_y = 35 \times 20$ pixels for each micropad. If the track is

assembled along y, we get a 35 × 860 pixels array that forms our practical signal $\overline{S}(i, j)$, thus an image of ~30 Kpixels. Hundred such arrays could be arranged on a biochip for multiplex biomedical sensing.

To exploit the case of stepped resonance conditions, we first form a correlation along the long dimension y of the sensed fluid image $\overline{S}(i, j)$ with the reference fluid image $\overline{S}_{\text{ref}}(i, j)$, yielding $C(\Delta j) = D_x^{-1}\Sigma_i\ \overline{S}(i,*) \otimes \overline{S}_{\text{ref}}(i,*)$. Each of the D_x lines (vectors) is correlated to the same line in the reference (~convolved with the reversed vector) and the sole average is made along the 35 = D_x pixels of the x direction. In a continuous version this correlation $C(\Delta j)$ would peak and be locally centered at a general (noninteger) pixel shift Δj_{sens} (directly proportional to the micropad shift Δm), accurately indicative of the sensed fluid index. However, with step functions, such a correlation $C(\Delta j)$ consists mathematically of straight segments meeting at angular points with maxima exactly pinned at micropad centers (think of the self-correlation of a unit square function Rect(y), which is a triangle function).

The solution to exploit the correlation beyond this maximum pinning effect is to privilege the determination of the centroid of the resonance peak in $C(\Delta j)$. This procedure would not be very accurate because the less controlled nonzero tails of the Fano resonance can have a large weight in this centroid determination, pulling the center of gravity far from the good value quite obviously. Our simple idea to cope with this issue is reminiscent of matched filtering, whereby the signal is privileged over the noise at chosen spectral locations. Here we have to privilege the peak of our resonance, and we should limit the impact of the "continuous" signal typical of a Fano line shape. We can make this simply by using higher powers of C and looking at the centroid of these higher powers. In our case, a function such as C^k with exponent k = 10 typically has a width comparable to the model's resonance width (2 to 4 micropads). We do not further justify the noncritical exponent value k = 10, a general theory of an optimal k amounts in some respect to the logic of matched filtering hinted above, too long to formalize here. Furthermore, if q is low and the shape asymmetrical, C features large flat "noninformative" regions of high signal whose noise blurs the centroid determination.

An example of a pair of asymmetrical reference and sensing signals with q = 2.5 is shown in the Figs. 4(a) and 4(b) with a shift value of ~60 pixels = 3 micropads, with a plot of their profile in Fig. 4(c). The correlation $C(\Delta j)$ is shown in Fig. 4(d). Given the absence of noise, the summation on the D_x lines is useless here. We see that the correlation peak is bounded by a high and flat plateau. Here no zero-padding was applied (we used fast Fourier-Transform), but even with zero-padding in a correlation there is a similar issue. This plateau does not help determining the shift through the search of the correlation centroid according to $\Delta j_{\text{sens}} = \Sigma\ \Delta j\ C(\Delta j) / \Sigma\ C(\Delta j)$. However, we see that going to C^k with a power adapted to the width of the signal, here k = 10, we adequately isolate the correlation peak. And thus the resulting curve lends itself well to a meaningful centroid calculation. The set of possible k values for such better behavior is reasonably large, starting at about k = 4, hence there is no practical constraint in this "adaptation" of k isolating the peak with usual RWG Fano shapes. We checked more precisely conditions for such a good match of centroid and maxima, and we found that for that purpose, removing the average of C^2 helps for a systematic treatment, by minimizing better the tails values and their influence compared to peak values: thus, we eventually deal with $C'^k = \left(C - \left\langle C^2 \right\rangle\right)^k$ instead of C^k, C being normalized to a maximum at unity. Thus, we have our shift counted in pixels determined by Eq. (3):

$$\Delta j_{\text{sens}} \approx \Sigma \Delta j C'^k(\Delta j) / \Sigma C'^k(\Delta j). \qquad (3)$$

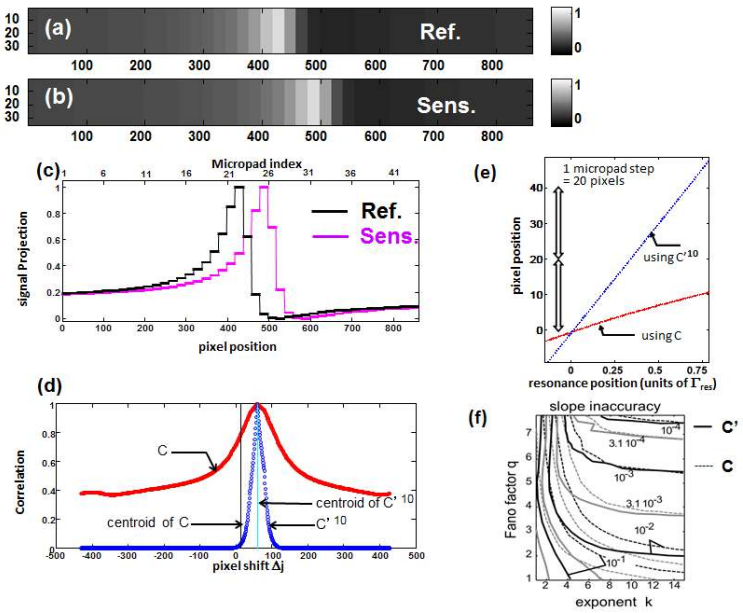

Fig. 4. Correlation and Fano signals (a) Fano resonance simulated image for reference medium and (b) Sensed medium; (c) Signal obtained by averaging over the lines for reference and sensed medium (d) Plot of correlation (solid line) and of powers of the biased version of correlation C'^{10} (dots). Calculated centroid position does not have the correct position for the centre; (e) retrieval of resonance position in pixel shift units. The centroid of C'^{10} has the right slope, whereas the centroid of C has its slope flattened; (f) Relative slope accuracy $\Delta S/S$ as a function of k and q in the case of C'^{k} (solid contours) or in the worse case of C^{k} (dashed contours).

We defer the mathematical analysis of such a treatment to further work, the important point being that retrieval through our tracking system can be highly resolved with a simple analysis that copes well with a highly asymmetrical Fano line shape.

The shape of C'^{10} in Fig. 4(d) with clear slope changes reveals the segmented nature of C that was not so apparent in C itself given the involved width of several micropads. Figure 4(e) gives the centroid position depending on resonance position, and eventually shows that the use of C'^{10} does retrieve a correct value with the adequate slope (Γ_{res} = 3.05 micropads = 61.0 pixels), whereas the naive use of C gives a much lower slope, due to the fact that C does not vanish at the edges of the segment (since the Fano line shape does not vanish), adding "unpredictable" weights in the centroid: such weights have for instance a heavy dependence on q.

A last confirmation and a guide to the optimization of this treatment can be deduced from the contour maps of the relative slope inaccuracy, Δ = (retrieved slope-ideal slope)/(ideal slope) on Fig. 4(f), as a function of k and q, for both cases C and C′. These contours compactly document the margin and the justification of our choices.

3.2. Robustness to Gaussian noise

We now illustrate the robustness of shift determination to noise still using signal with Fano shapes of parameter q = 2.5, but adding a large contribution of Gaussian noise. Resulting images and profiles are given in Figs. 5(a)–5(c). Noise was added on pixels $\overline{S}(i,j)$ as constant noise $\overline{S}_N$ of rms value σ_S = 0.3 (e.g. readout noise, the model pixel values are here assimilated to reflectivities $0 < \overline{S}(i,j) < 1$). In addition a photon noise was mimicked by introducing a factor $\overline{S}_{N,\mathrm{phot}}$: $\overline{S}(i,j) = \overline{S}_{\mathrm{perfect}}(i,j)(1+\overline{S}_{N,\mathrm{phot}})$ with the same rms noise σ_N = 0.3

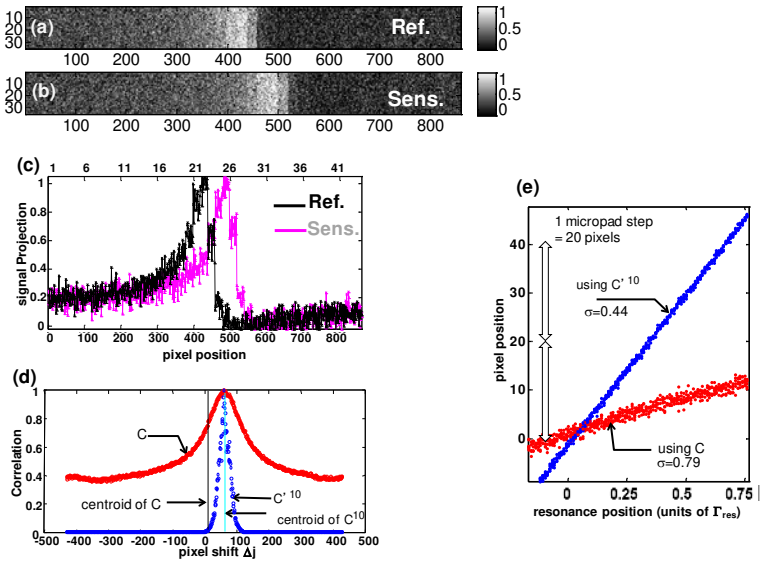

Fig. 5. Simulated reference and sensing tracks in the presence of a large noise (signal-to-noise ratio ~1 at the pixel scale) (a) for reference track and (b) for sensed track; (c) Signal obtained by averaging over the lines for reference and sensed media; (d) Plot of correlation C (solid line) and of power of the biased version of correlation C'^{10} (dots) ; (e) retrieval of resonance position in pixel shift units. The rms fluctuation in pixel units is 0.79 in the former case, with also a still inadequate slope, and 0.44 in the second case.

for $\overline{S}_{N,\mathrm{phot}}$. Hence the pixel-scale signal-to-noise ratio (SNR) barely reaches 2 at resonance, but the 700 pixels of each micropad make the SNR ~ $\sqrt{700}$ ~ 25–30 times better. Already, the projections on Fig. 5(c) show SNRs ~ 10. Figure 5(d) shows the impact of this noise on the correlation $C(\Delta j)$, which is noisy. To check how good the retrieval is, we performed a set of 6 simulations at a series of shifts Δm and get the data of Fig. 5(e): a linear determination with a narrow rms deviation of σ = 0.44 pixel = 0.02 micropad is obtained using C'^{k} with k = 10, whereas a larger rms noise of σ = 0.79 pixel = 0.039 micropad is obtained for the direct use of C, in addition to the skewed slope already commented (again Γ_{res} = 3.05 micropads = 61.0 pixels). Considering the low initial SNRs, this result demonstrates high robustness to noise and thus potential real-time capability.

3.3. Robustness to in-homogeneities resulting from imaging

Next, we examine the robustness of our procedure in the presence of an imaging defect, i.e., if the micropad intensities are not uniform (within Gaussian noise) but are seen with some spatial distortions due to any aberration. Another possible cause of distortion could be a fabrication issue that would cause the local resonance parameter to shift away of its nominal value at the edges of the micropad. A third and more complex issue is the spread of the waveguide mode across micropads due to mode propagation [5]. As said above, we discard such crosstalk by orienting the guided wave normal to the tracks.

We choose to exemplify here the fabrication variability aspect. This is also the main contribution we observed experimentally. For instance, in an electron-beam lithography process, unless being finely mitigated through coding or software, lower exposure occurs at the edge of the pattern. The micropads signals are thus blurred by an internal spatial shift of the resonance value, with nontrivial consequences on the intensity values. We assign a sizable value for the maximum nonuniformity inside a micropad, namely associated to Δm = 3.5, as though the duty-cycle had a local value inside a given micropad reaching the designed one for 3.5 micropads away. We made the shape of the distortions qualitatively resembling some of

the imperfect images that we obtained experimentally (Section 4). Figures 6(a)–6(d) present the results with essentially the same reference Fano shape as Figs. 4–5, the value q = 2.5 being kept again.

Figure 6(e) gives a colormap of the normalized micropad perturbation, essentially an elliptically-shaped rise of the local resonance parameter. We took the same perturbation on all micropads. Admittedly, this is not as realistic as it could be, but, conversely, there can be a common biasing trend to all micropad grating parameters, and the dominance of a long-range variation at the whole track scale is still the more likely scenario. Figures 6(a) and 6(b) give two views of reference and sensing situations, here with smaller noise σ_s = 0.06 (still with Gaussian and photon noise contributions) compared to the previous case σ_s = 0.3. Figure 6(c) gives the plot along the y axis of the x-projected signal $\overline{S}(i,j)$, $\Sigma_i \overline{S}(i,j)$, with clear departures from the constant plateau, suggesting possible extra induced difficulties if a fit of standard nature were to be applied. Figure 6(d) gives the correlation of track and sensing tracks with details on C and C'^k as in Figs. 4-5. Figure 6(d) shows that the correlation still works well, hence we have identified another robust aspect of our method. To check this at a larger level, Fig. 6(f) eventually gives the retrieval of the shift Δj with the same conventions as in Fig. 5. The bias (less than 1 pixel) is only a systematic one following the contribution of the perturbation, but the linearity with a correct slope is fully preserved. The bias is indeed on the order of a couple of standard deviations associated to this noise level, σ = 0.087 pixels = 0.0043 micropad unit.

Overall, the noise of this method is acceptably low. Having given in Section 2 the general philosophy and main design aspects of our peak-tracking chip, and having given a generic data treatment based on correlation that appears to perform well against a number of adverse effects (Fano line shape, pixel-scale noise, micropad-scale distortions), we now apply it to experimental sensing. In Section 4, we demonstrate that very accurate index sensing results from the combination of the design and the particular flavor of correlation analysis benchmarked above.

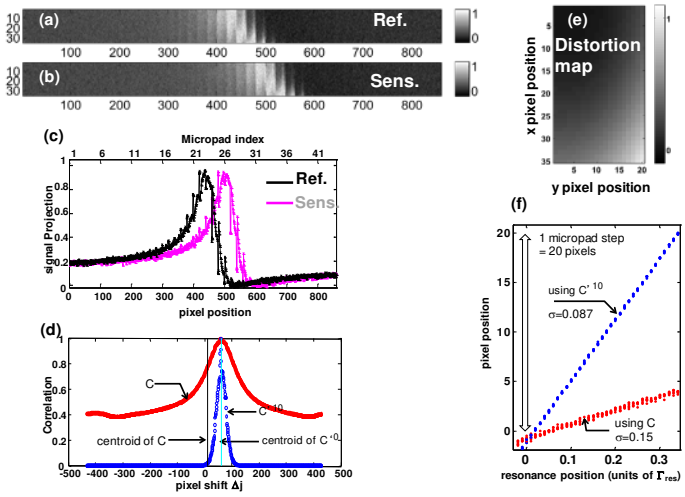

Fig. 6. (a), (b) Distortion simulation. Each micropad is assumed to suffer from an internal distortion of its resonance position corresponding to 3.5 micropad unit, with the smooth normalized pattern shown in (e). (c) Projection on y averaged over the lines (d) Correlation functions C and C'^{10}. The rms noise remains below the tenth of pixel limit. (e) Distortion map. (f) Retrieval performances through the centroids of functions C and C'^{10}.

4. Experimental section

4.1. Experimental setup and process

In Fig. 7(a), we give a scheme of our experimental imaging setup. The sample is illuminated with green monochromatic light under an incident angle $\theta = 18°$. This choice also allows a $\sqrt{2}$ noise reduction through RGB coding. Further multi-parameter optimization of gratings micropads or other nanostructure might be realized [20,21], not necessary in the scope of this demonstration. It is illuminated from the glass side, so the incident angle on the RWG is not influenced by the analyte. To avoid laser speckle and enable incident wavelength optimization capability, we choose a white LED and select the wavelength with a monochromator. Specifically, the source is a high power LED from Thorlab Inc. It is filtered using a SSM 301 monochromator from Zolix instrument Co. Ltd. of Czerny-Turner configuration, with a 1200 grooves/mm grating and a focal length of 300 mm. The entrance and exit slits are adjusted to a width of 20 µm, hence a spectral width $\Delta\lambda \sim 0.2$ nm. A 150 mm lens then collimates the light from the exit slit, giving an angular resolution of 0.008°. These limited angular and spectral spreads guarantee an almost negligible influence on our ~5 nm full-width at half maximum (FWHM) resonance response with 5.5 nm/degree dispersion.

We first present results for large Δn span [1.333-1.474] (step $\Delta n = 0.028$) before discussing highly sensitive sensing within the restricted range [1.333-1.337] for steps $\Delta n = 0.001$. For the small Δn span between 1.333 and 1.337, we choose a wavelength of $\lambda = 545$ nm, while for the larger span range Δn from 1.333 to 1.474, the wavelength is adjusted to $\lambda = 558$ nm. With an experimental dispersion of 0.7 micropad shift equivalent to 1 nm spectral span, this change of wavelength allows to change the resonance peak position from micropad $m \sim 29$ to $m \sim 10$ and be able to cover the whole range of optical index [1.333-1.474] in the same optical configuration (same incidence angle). Adjusting wavelength instead of angle is more reliable considering the influence of mechanical motion in resonant optics experiments. Considering a quasi linear behavior of the resonant structure when varying a parameter on a small interval range, this wavelength adjustment has nearly no influence on the shift values measured in experiments.

Concerning data acquisition, to exploit 90% of the camera dynamics with our resolution of $\Delta\lambda = 0.2$ nm and $\Delta\theta = 0.008°$, we use a 1 sec integration time. Raw images are recorded by a Canon EOS 5D camera and are converted to 16 bits RGB tiff format giving a digitization relative precision of $\sim 2 \times 10^{-5}$. To limit data storage and avoid noise from the red and blue channels, we select only the green one. Each grating micropad is imaged on an area of 1000 to 2000 pixels; we average over 10 successive pictures, thus increasing the SNR by a factor of $100 \sim (10 \times 1000)^{1/2}$. Considering a typical relative noise of 4×10^{-3}/image on our camera pixels, the noise contribution is decreased to 4×10^{-5} in relative terms, around the digital accuracy for a typical signal with 2.5×10^4 counts.

In view of fluid sensing, the chip is mounted into a black-anodized aluminum holder having 2 separate chambers, with tubing connections on the fluid side, opposite to optics. The chip is held by the external pressure of a flange and serves as cover. O-ring joint are used to ensure hermetic sealing between the holder and the chip. Once the chip is fixed on the holder, water is introduced in one of the chamber and will serve as the reference (mechanical motion…). The other chamber is used to sense the various analyte successively injected in it. In order to limit vibrations, we use a syringe pump with a flux of 150 µL/min, and wait for 10 min between each of the measurement to allow the sample to reach the chamber with enough subsequent time for stabilization. Such a slow flow is also chosen to avoid temperature increase and a possible subsequent thermo-optic effect.

4.2. Large span Δn sensing

We first present experimental data measured for the large Δn span from 1.333 to 1.474 by $\Delta n = 0.028$ steps. Analytes are prepared using prescribed fractions of glycerol and water. For the

high refractive index variation, we prepared the following water/glycerol solutions: 1:0, 80:20, 60:40, 40:60, 20:80, 0:1.

After chip picture acquisition, we determine profiles for both reference and sensing tracks. In a perfect case (ideal and stable experimental setup), the reference track image should be invariant throughout the sequence. However, small variations are measured, possibly due to pressure stress, and used for shift correction, making the procedure quite immune to drifts. Images corresponding to each of the indices as well as one of the reference images are shown in Fig. 7(b), and their averaged profiles are reported in Fig. 7(c), the line between points being only a guide to the eye. Concerning the profiles, only 30 × 40 pixels of the center of the micropads (of size ~35 × 50 with present magnification) are considered, therefore limiting fabrication variability contribution. Reference and sensed tracks profiles are then fitted with Lorentzian and Gaussian model and the resulting resonant shift is reported in Fig. 7(d). As seen in Section 2 (Fig. 2(d)), peak position on this large refractive index span has slight curvature that might be calibrated for sensing purpose. The peak position may however be considered as locally linear for small refractive index sensing span. Peak position determination confirm that all 5 first control tracks pictures yield very similar profiles (blue lines, variation of peak position $\Delta m \sim 0.015$) but the last one is shifted towards the left by $\Delta m = 0.6$. Indeed, higher pressure, needed when injecting the viscous glycerol solution may have resulted in mechanical instability and chip motion, which confirms the advantage of using a reference.

We also perform resonant position determination using correlation analysis. The sensed track is correlated to the referenced track for each analyte. Shifts values are reported in Fig. 7(d) and are in agreement with the other fits. Difference between the different fitting methods will be discussed with the next set of data for highly sensitive sensing.

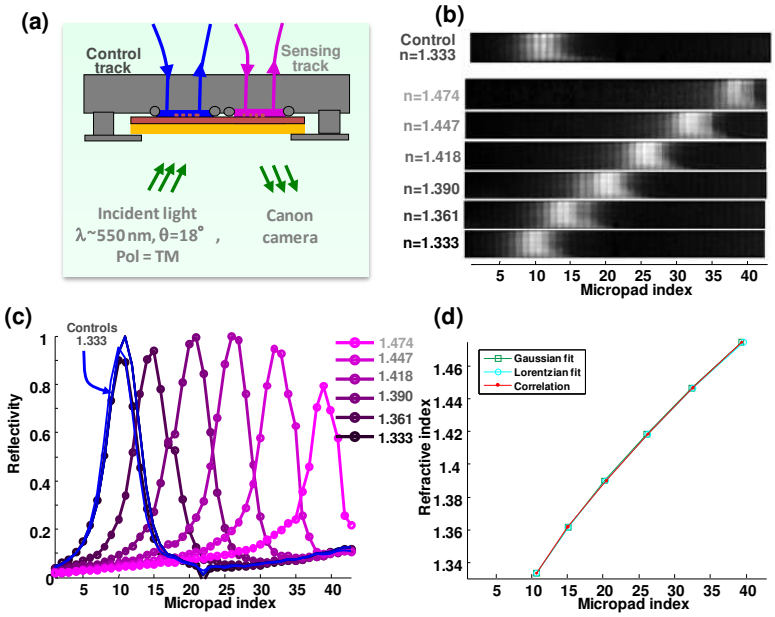

Fig. 7. (a) Scheme of the experimental setup composed of a source monochromatically filtered and polarized, illuminating a chip with 2 tracks, one serving as reference and the other for sensing, and a camera to image the chip (b) Measured images of one of the reference picture and media with index from n = 1.333 to n = 1.474 (c) Reflectivity profiles for each of the reference (blue) and of each of the media (n = 1.333 to n = 1.474) (d) Reported peak position determined by Gaussian fit (green), Lorentzian fit (cyan) and correlation analysis (red). The measured resonance position is plotted in abscise axis and the known refractive index of the solution in ordinate axis.

The total measured shift is $\Delta m \sim 29$ micropads being therefore lower than the expectation $\Delta m \sim 37$. This might be partly explained by lower dispersion, for instance associated to deeper etching than the 0.15Λ targeted value or scattering loss through porosity in the silicon nitride. Another aspect is the slightly higher Δf step vs. the designed filling factor variation, as seen from our SEM measurements, reducing the discretization by ~3 micropads on the considered interval, leaving thus a reasonable agreement between theory and experiments.

4.3. Highly sensitive sensing on reduced Δn span

We finally study sensitivity through a small refractive index span, with refractive index variation $\Delta n = 10^{-3}$ between 1.333 and 1.337 by using water/glycerol solutions in ratio 1:0, 0.993:0.007, 0.986:0.014, 0.979:0.021, 0.972:0.028. The latter solutions are prepared with double dilution to get accurate concentration steps. In Fig. 8 we give (a) the measured images and (b) there profiles. Looking carefully at the pictures, we see that when the refractive index increases, the maximum is shifted towards micropads of higher number. This is clearly confirmed when looking at the reflectivity profiles. In Fig. 8(c) we give the correlation result of the first image for n = 1.333 (reference of sensing track) with images of index between 1.333 and 1.337, the first curve corresponding to reference.

In Fig. 8(d), we report the resonant peak shifts determined by different fitting methods. Peak position versus nominal refractive index displays a fairly nice linear trend on the reduced interval [1.333-1.337]. The slope, however, depends on the fitting/correlation analysis and can be determined numerically. We report the corresponding lines (black color) in Fig. 8(d) for each of the methods, and all three fits are nearly indistinguishable from their associated data subset. The inset presents the deviation from the nominal refractive index to the one which would correspond to the fractional micropad position, i.e. the remaining error

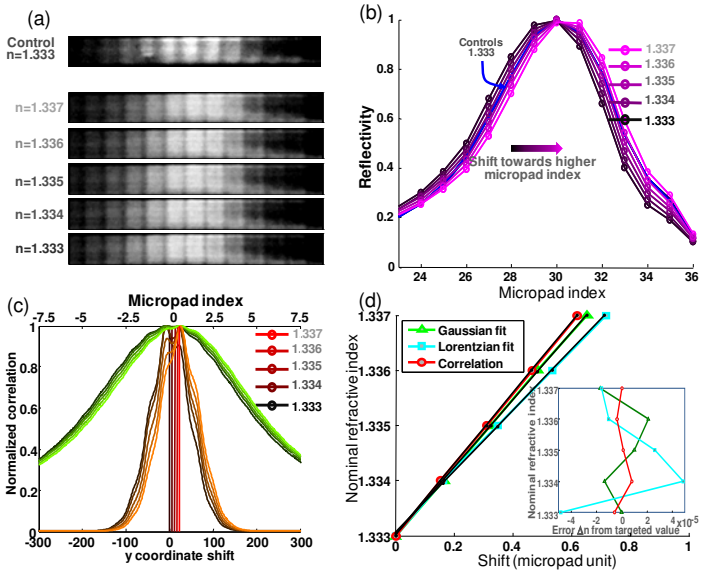

Fig. 8. (a) Images of tracks for micropads from 24 to 36, both for reference and sensed solution for indices from 1.333 to 1.337 by step $\Delta n = 10^{-3}$ (b) Experimental profiles using central pixels of micropads and plotted as line profile for visual convenience (c) Normalized correlation C (greenish broad bell-shaped) and C'^{10} (brownish narrower) curves, as well as centroid center position (reddish vertical lines).(d) Shift of the peak determined by Gaussian and Lorentzian fits as well as correlation analysis. Different fits and the correlation method give aligned points whose fitted slope can be used as index transduction calibration. The inset gives the error with respect to the fitted slope trend, plotted in abscissa vs. the analyte refractive index (ordinate), for all three analyses. Errors are on the order of a few 10^{-5}, thus a few percent of the 10^{-3} index step.

with an affine fit having the slope of the data subset just mentioned above. For the correlation approach, the residual error observed demonstrates that a precision of index (RIU) sensing down 2×10^{-5} RIU can be achieved. The same error analysis conducted with Gaussian fit or Lorentzian fit give much more spread errors. The amplitude of the variations (inaccuracy) in the fit are not on the order seen in Fig. 3(a), but we look at only a small span of less than 1 micropad. Our data also have a ~twice larger full width at half maximum (~6.5 micropads) and are less asymmetric than expected from our simulated reflectivity profiles.

5. Conclusion

In this paper, we demonstrated a highly sensitive and self-referenced refractive index sensing technique using a new principle involving tracks of RWG micropads with neighboring resonant conditions, imaged by a fixed commercial consumer-grade camera. Refractive index variation is retrieved from the sole image analysis. Common wide field imaging of such camera leaves ample room for multiplex detection with a bidimensional disposition of tracks accommodating $N \times P \sim 100$ arrays [22]. Resonance properties in each track are tuned through the grating pattern geometry. Technology limits to the fine trimming give rise to discrete variations nearly at the resonance width scale and therefore discretized profiles, which need to be fitted for precise refractive index determination.

A critical aspect of refractive index sensing, especially for biological applications, is sensitivity. This aspect is limited by the interplay of digitization itself and the capability to accurately analyze the measured profiles. Our technology-limited filling factor step of $\Delta f = 0.0089$ with green light and period $\Lambda = 450$nm, gives a dispersion of $\sim 4 \times 10^{-3}$ RIU/micropad. Therefore, fine data analysis is necessary to attain sensitivity down to $\sim 10^{-5}$ RIU range.

This issue can be addressed using a specific correlation approach. By correlating the sensed track image with a reference track image (either the same track for a prior reference time or a control track on the same picture accounting for all systematic time-dependent variations), we can retrieve resonance position. Accurate retrieval requires using an offset and a higher power ($k \geq 4$) of the correlation and extracting the centroid of the result. This correlation approach was compared to usual fitting techniques (Lorentz, Gauss) and demonstrated superior robustness to asymmetry of the profiles, as well as to diverse parasitic contributions influencing measured signals. Such parasitic contributions may have different origins, such as fabrication (electron beam lithography exposure varies at the edge of the pattern), optical aberration. For instance, to improve the initially poor success of Gaussian and Lorentzian fitting, we had to clip only pixels in the middle of the micropads, while for correlation analysis the whole track could be considered without harm. This is a significant advantage for the analysis as micropad pixel coordinates do not have to be determined.

A good sensitivity was demonstrated through experiments using glycerol/water analyte solutions with 5 steps of $\Delta n = 10^{-3}$, giving an accuracy of $\Delta n \sim 2 \times 10^{-5}$. This sensitivity is typically equivalent to that of a ~20 pg/cm^2 density biological layer. This makes our technique a promising candidate for robust and accurate multiplex label-free bio sensing.

The robustness and simplicity of our correlation approach may be used for other RWGs technique to exploit data on the fly in real-time conditions. Indeed, there appears to be a substantial room to reduce exposure time, thus decreasing the pixel-scale SNR, while still preserving (i) the high sensitivity stemming notably from the full exploitation of the picture rooted in the correlation approach and (ii) the accuracy brought by the same-image referencing. This result indicates more generally that coarse discretization in spectrum may be best exploited with procedures of the "match filtering" family. Our specific correlation approach for profile analysis may therefore be adapted to peak shift determination in usual spectral or angular RWGs based detection techniques [2–4,7].

The correlation approach for precise analysis was therefore demonstrated successfully and its many significant advantages were benchmarked. It is also compatible with video rate

experiments from the image treatment viewpoint, as the algorithm for correlation can be implemented using fast Fourier transform rather than convolution.

In summary, this work provides the first substantiated demonstration of ultra-sensitive on-chip determination of optical resonance peak position tracking using a correlation approach. The "peak-tracking chip technique" was successfully applied to track a liquid analyte's index of refraction through the peak spatial position associated to step-wise variation of one of the grating parameters. The duty-cycle variation was chosen here to allow multiplex track disposition as well as reasonable discretization through micropads of variable groove width, demonstrating a sensitivity of ~2×10^{-5}. A correlation analysis was found to be crucial for the obtainment of such accuracy from the discretized micropad data. This ensemble suggests that the peak-tracking chip scheme has a great potential in the field of biodetection.

Acknowledgments

The electron beam lithography project was supported by Hong Kong University of Science and Technology Grants SEG_HKUST10. The project is supported by RGC grant number 604710 as well as grant RPC11SC01. The authors are grateful to HKUST nanofabrication facilities staff for their help in the chip fabrication process, and more particularly to K. C. Li and M. W. Lee. We thank as well L. Wang, Y. Zhang and S.K. Cheung for fruitful discussion on fluidic integration and experiment stabilization.